FULL PAPER

# Nucleus-Targeting Gold Nanoclusters for Simultaneous In Vivo Fluorescence Imaging, Gene Delivery, and NIR-Light Activated Photodynamic Therapy

*Raviraj Vankayala, Chien-Lin Kuo, Karthik Nuthalapati, Chi-Shiun Chiang, and Kuo Chu Hwang**

**The nucleus is one of the most important cellular organelles and molecular anticancer drugs, such as cisplatin and doxorubicin, that target DNA inside the nucleus, are proving to be more effective at killing cancer cells than those targeting at cytoplasm. Nucleus-targeting nanomaterials are very rare. It is a grand challenge to design highly efficient nucleus-targeting multifunctional nanomaterials that are able to perform simultaneous bioimaging and therapy for the destruction of cancer cells. Here, unique nucleus-targeting gold nanoclusters (TAT peptide–Au NCs) are designed to perform simultaneous in vitro and in vivo fluorescence imaging, gene delivery, and near-infrared (NIR) light activated photodynamic therapy for effective cancer cell killing. Confocal laser scanning microscopy observations reveal that TAT peptide–Au NCs are distributed throughout the cytoplasm region with a significant fraction entering into the nucleus. The TAT peptide–Au NCs can also act as DNA nanocargoes to achieve very high gene transfection efficiencies (≈81%) in HeLa cells and in zebrafish. Furthermore, TAT peptide–Au NCs are also able to sensitize formation of singlet oxygen ($^1O_2$) without the co-presence of organic photosensitizers for the destruction of cancer cells upon NIR light photoexcitation.**

## 1. Introduction

Cancer is considered to be one of the most challenging threats leading to the human deaths.[1] Although therapeutic approaches, such as radiotherapy and chemotherapy, were developed in the clinics to treat cancer, most of them were not effective, as the drugs mainly translocate into the intracellular endosomal or lysosomal compartments rather than inside the nucleus. For an effective therapeutic treatment, nucleus targeted entry into the cancer cells is an essential factor.[2] Nucleus is considered to be the most hypersensitive intracellular organelle because the genetic information of the cell and transcription machinery resides at that location. The major biological function of the cell nucleus is to maintain the integrity of genes by regulating its genetic expression.[2,3] Ideally, molecular anticancer drugs targeting at the DNA inside nucleus are considered to be more effective on killing cancer cells than those targeting at cytoplasm or other intracellular organelles.[2,3] However, due to the limited access of the cytosolic drugs able to enter the nucleus, it becomes highly impossible for drugs/genes to achieve nucleus-targeting and exert subsequent therapeutic effects.

In the recent years, the development of nanotechnology has made significant advancement in the fields of clinical biomedicine. A numerous varieties of nanomaterials were reported, such as gold, silica, polymeric, and liposomal nanoparticles, to facilitate as drug/gene carriers to cancer cells.[4–6] In order to achieve nucleus-targeting properties using large hydrodynamic size nanoparticles, efforts were devoted to modifying the surface of the nanoparticles using nucleus localization signal (NLS) peptide. However, such nanoparticles have ended up with very low percentages of nuclear entry due to their large hydrodynamic sizes. Alternatively, semiconducting quantum dots (QDs), dye-doped nanoparticles, upconversion nanoparticles, silicon quantum dots, graphene quantum dots. and carbon dots were also developed with ultrasmall hydrodynamic diameters.[7–10] Although, these nanomaterials were proven to be effective in various biomedical applications, such as drug/gene delivery, their intracellular fate in relation to the nucleus-targeting properties has not been explored.

Recently, noble metal nanoclusters (NCs) has attracted significant attention, since they are composed of roughly hundreds of atoms and exhibit an artificial molecule-like property along with size tunable photoluminescence.[11–13] Among various noble metal nanoclusters, gold nanoclusters (Au NCs) of size ≈2 nm are promising, owing to its excellent chemical stabilities, bright photoluminescence properties and appreciable biocompatibilities.[11,12] Although, Au NCs were widely used as a nanocarrier to carry molecular drugs or genes, their abilities to target nucleus and its subsequent therapeutic effects on killing cancer cells largely remain unknown.[14] Therefore,

Dr. R. Vankayala, Dr. C.-L. Kuo, K. Nuthalapati, Prof. K. C. Hwang
Department of Chemistry
National Tsing Hua University
Hsinchu 30013, Taiwan
E-mail: kchwang@mx.nthu.edu.tw
Prof. C.-S. Chiang
Department of Biomedical Engineering and Environmental Sciences
National Tsing Hua University
Hsinchu 30013, Taiwan

DOI: 10.1002/adfm.201502650

an effective multifunctional theranostic nanoplatform capable of targeting the cell nucleus for the diagnosis and treatment of cancer is urgently wanted.

Photodynamic therapy (PDT) is one of the noninvasive therapeutic strategies, where organic photosensitizers (PS) and light are employed to induce cellular death and tissue destruction.[13] In the conventional organic PS-mediated PDT, the PS molecules absorb and transfer incident photon energy to the surrounding oxygen molecules and generate cytotoxic reactive oxygen species (ROS), such as singlet oxygen ($^1O_2$), superoxide, hydrogen peroxide, and hydroxyl radicals, to cause irreversible damage to the biomolecules including DNA, proteins, and lipids.[15,16] However, such type of organic PS-mediated photoinduced destruction of cancer cells has limited effects, as the organic PS molecules failed to accumulate and target at the nucleus. In general, the therapeutic outcome of the PDT is strongly dependent on how and where the ROS interact and target at various subcellular organelles such as endosomes, lysosomes, mitochondria, nucleus, etc.[17] Direct targeting at the nucleus and damaging the DNA by ROS are considered to be the most effective pathways of PDT. Due to their very high chemcial reactivities, ROS species produced within the subcellular compartments, in general, have very short lifetimes (<200 ns), and a very short diffusion ranges (≈20 nm) and will react with proteins and DNAs in the neighborhood sites where they are generated (via photoexcitation of photosensitizers).[18,19] In this regard, the cell nucleus is considered to be a hyper-sensitive site for the effective PDT-mediated damages to occur. It is highly difficult and challenging for organic PS molecules to selectively target at the cell nucleus and facilitate nucleus-targeting PDT. Previously, protein-stabilized gold nanoclusters and gold nanoclusters embedded in the polymer matrix were known to sensitize formation of singlet oxygen upon photoexcitation of 330 nm UV light and 532 nm visible light, respectively.[20,21] Very recently, thiolated gold nanoclusters ($Au_{25}$ $(SR)_{18}$) were known to sensitize formation of singlet oxygen upon photoexcitation of visible light (532 and 650 nm) or short near infra-red light (808 nm) and exert cellular deaths.[22] Although cellular deaths were observed, their abilities to target nucleus, intracellular generation of ROS, and nucleus targeting photodynamic therapeutic effects were not reported.

In this study, we report that, (1) alkyl thiolated gold nanoclusters (RS–Au NCs) and nucleus-targeting gold nanoclusters (TAT peptide–Au NCs) can be effectively uptaken by HeLa cells and distributed evenly surrounding the cytoplasmic region, with the significant fraction entering into the nucleus; (2) RS–Au NCs and TAT peptide–Au NCs are biocompatible toward HeLa cells and does not induce any significant abnormalities in zebrafish; (3) the red emitting RS–Au NCs and TAT peptide–Au NCs were homogenously distributed from the yolk-sac region to tail in the zebrafish; (4) RS–Au NCs and TAT peptide–Au NCs can also act as DNA cargoes with ultrahigh gene transfection efficiencies (≈81%) in HeLa cells, which is nearly 3.2-fold higher than that obtained using the most commonly adopted LP2000 liposome gene carrier; (5) upon long (850–1100 nm) near-infrared (NIR) light excitation, RS–Au NCs can sensitize formation of singlet oxygen and exert nucleus-targeting nanomaterial-mediated PDT effects on killing cancer cells. Overall, such unique design of nucleus-targeting multifunctional gold nanoclusters for simultaneous fluorescence imaging, gene delivery, and long NIR light activated PDT has a great potential in the future clinical treatment of cancers.

## 2. Results and Discussion

### 2.1. Synthesis and Characterization of RS–Au NCs and TAT Peptide–Au NCs

The synthesis of RS–Au NCs was carried out in two steps by using a simple ligand exchange approach with 11-mercaptoundecanoic acid (see **Figure 1**). The crude products were a mixture of nanoparticles and nanoclusters. Through an ultracentrifugation process, large-sized nanoparticles can be removed and separated from small nanoclusters. To introduce nucleus-targeting properties to the gold nanoclusters, the amino group of the TAT peptide (peptide sequence: N-GRKKRRQRRR-C) was conjugated to the terminal carboxylic group of gold nanoclusters via EDC (1-ethyl-3-(3-dimethylaminopropyl) carbodiimide) coupling reaction (see step-3 in Figure 1). The UV–vis–NIR absorption spectra for both RS–Au NCs and TAT peptide–Au NCs clearly reveals monotonic absorption covering the entire spectral range until 900 nm with significant absorption being in the range of 200–400 nm (see **Figure 2**A). However, the absorption spectrum for TAT peptide alone exhibits a single band centering at 220 nm wavelength. The photoluminescence spectrum of RS–Au NCs exhibits a characteristic emission peak centering at 610 nm upon 365 nm light photoexcitation. Upon conjugation with the TAT peptide, a slight blueshift was observed in the emission wavelength, which was centered at 600 nm. Upon exposure to UV light (365 nm), both RS–Au NCs and TAT peptide–Au NCs aqueous solutions exhibit bright red fluorescence (see inset in Figure 2B). The successful functionalization of TAT peptide on the surface of RS–Au NCs was also confirmed by FT-IR spectroscopic analyses (see Figure S1, Supporting Information). The RS–Au NCs exhibit significant —O—H stretching at 3126 $cm^{-1}$, due to the carboxylic acid groups of 11-mercaptoundecanoic acid. However, upon conjugation of TAT peptide, a prominent amide —C=O stretching and —CO—NH stretching appear at 1664 and 1537 $cm^{-1}$, respectively. The structure of the RS–Au NCs was examined using transmission electron microscopy (TEM) (see Figure 2C). The inset in Figure 2C represents the higher magnification TEM image of RS–Au NCs. The average particle size of RS–Au NCs is 3–5 nm. The matrix-assisted laser desorption ionization (MALDI) mass spectrum in Figure 2D shows a dominant molecular ion peak of m/z at 2100, which was consistent with the presence of eight gold atoms. In order to estimate the surface chemical composition of gold nanoclusters, X-ray photoelectron spectroscopy (XPS) was used to measure the characteristic binding energies. The high resolution (HR) XPS for Au 5f deconvoluted spectrum of RS–Au NCs in Figure S2A (Supporting Information) shows two peaks at binding energies 83.9 and 87.7 eV, which are corresponding to Au $5f_{7/2}$ and Au $5f_{5/2}$ of Au (I), respectively. Figure S2B (Supporting Information) represents the deconvoluted spectrum of S 2s, which clearly exhibits two separated peaks attributed to

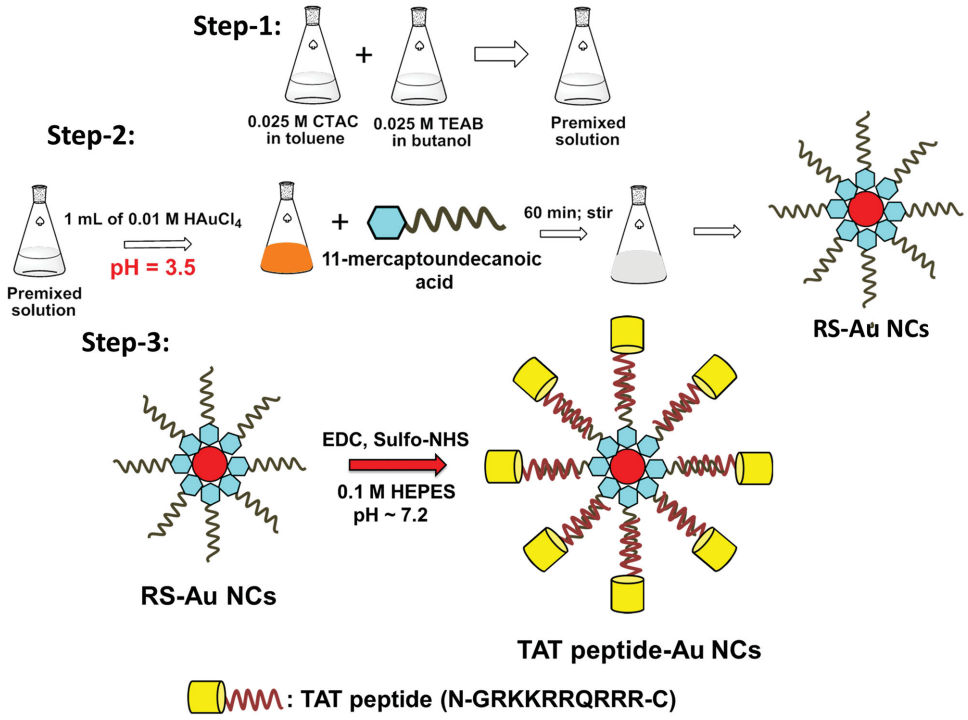


**Figure 1.** Schematic representation for the synthesis of red emitting RS–Au NCs and TAT peptide–Au NCs, respectively.

the Au–S at 161.3 eV and S–S at 163.3 eV, respectively. The photostabilities of the red fluorescent RS–Au NCs were also compared with that of conventional organic dyes (see Figure S3, Supporting Information). The result shows that RS–Au NCs possesses much better photostability as compared to the organic dyes, such as fluorescein isothiocyanate (FITC).

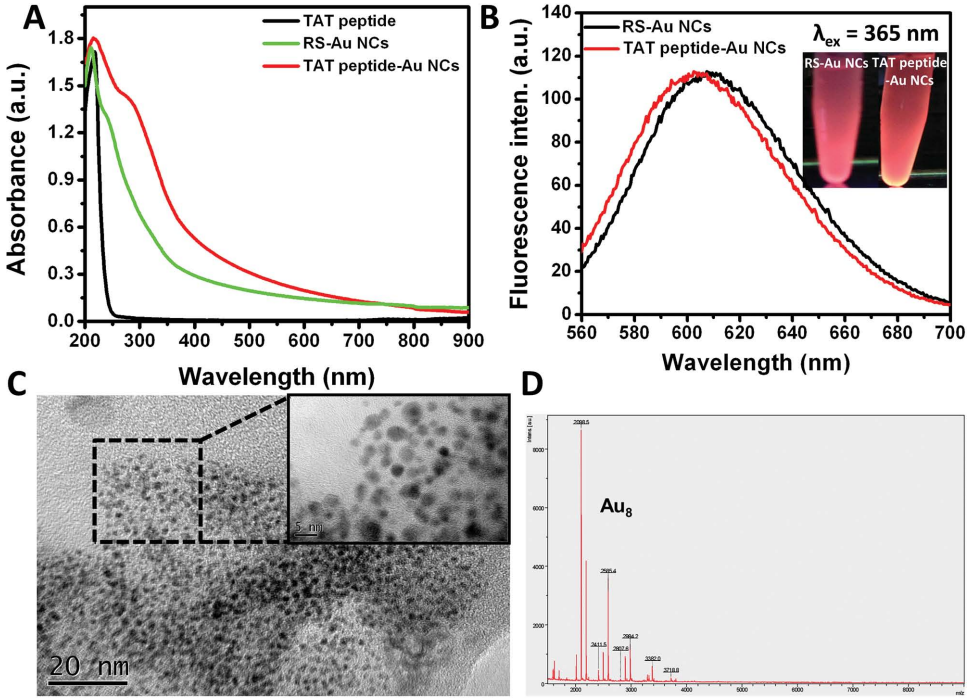


**Figure 2.** A) UV–vis–NIR absorption spectra for red fluorescent RS–Au NCs, TAT peptide alone, and TAT peptide–Au NCs. B) Photoluminescence emission spectra for red fluorescent RS–Au NCs and TAT peptide–Au NCs. The inset photographs represent the fluorescence images of red emitting RS–Au NCs and TAT peptide–Au NCs, using 365 nm as the excitation wavelength. C) TEM image of RS–Au NCs. The inset represents the high resolution TEM image. D) MALDI mass spectrum of RS–Au NCs.

### 2.2. In Vitro Cellular Uptake and Cytotoxicity of Lipid-Coated Au Nanoclusters

To achieve efficient gene/drug delivery or nucleus-targeting photodynamic therapy, it is mandatory for the cancer cells to have very high intracellular uptake of nanomaterials.[11–13,23–25] To this end, we first evaluated the cellular uptake of RS–Au NCs and TAT peptide–Au NCs in HeLa cells by measuring their characteristic red fluorescence using confocal laser scanning microscope (CLSM) and flow cytometry. The confocal images in **Figure 3**A clearly show that most of the red fluorescence emitting from RS–Au NCs were evenly distributed surrounding the cytoplasm region with a very less fraction being entered into the nucleus. However, for the confocal images of HeLa cells pretreated with TAT peptide–Au NCs, majority of the red fluorescence was clearly observed inside the nucleus (see lower panel confocal images in Figure 3A). The confocal z-stacking images of TAT peptide–Au NCs internalized HeLa cells taken at different depth intervals were shown in Figure S4 (Supporting Information). The mean fluorescence intensities of both RS–Au NCs and TAT peptide–Au NCs internalized HeLa cells were quantified in the cytoplasm and nucleus of the HeLa cells (see Figure S5, Supporting Information). It was very clearly evident that the TAT peptide–Au NCs internalized HeLa cells exhibit significantly higher percentage of intranuclear uptake rather than RS–Au NCs internalized HeLa cells. The line profiles in Figure 3B,C clearly indicate that the location of red fluorescence emission is inside the nucleus. The cellular uptake percentages were also determined using flow cytometry after HeLa cells were fed with various concentrations of RS–Au NCs and TAT peptide–Au NCs for 3 h (see Figure S6, Supporting Information). Overall, ≈90% cellular uptake efficiencies were observed for both RS–Au NCs and TAT peptide–Au NCs internalized HeLa cells under serum-free conditions in a concentration dependent manner. To examine the cytotoxicity of RS–Au NCs and TAT peptide–Au NCs in HeLa cells, MTT (3-(4,5-dimethylthiazolyl-2)-2,5-diphenyltetrazolium bromide) cell viability assay was performed. The cellular viabilities in **Figure 4**A clearly show that the RS–Au NCs and TAT peptide–Au NCs induce dose-dependent cytotoxicity behavior. The half maximal inhibitory concentration ($IC_{50}$) value of RS–Au NCs for HeLa cells is >75 μg $mL^{-1}$, whereas for TAT peptide–Au NCs, the $IC_{50}$ value is 50 μg $mL^{-1}$. Figure 4B shows the lactate dehydrogenase (LDH) assays for RS–Au NCs and TAT peptide–Au NCs. LDH is a characteristic assay to assess the membrane integrity of cells in the culture medium. When HeLa cells were exposed to different concentrations of RS–Au NCs and TAT peptide–Au NCs, the LDH levels were slightly higher than the control group. In particular, at higher concentrations of RS–Au NCs and TAT peptide–Au NCs, approximately threefold of higher LDH levels were observed as compared to the background level. Exposure of nanomaterials may cause generation of ROS inside cells.[26–28] To examine the induction of oxidative stress by RS–Au NCs and TAT peptide–Au NCs, we monitor the cellular ROS generation by flow cytometry using a nonfluorescent 2,7-dichlorofuorescein diacetate (DCFH-DA), which can

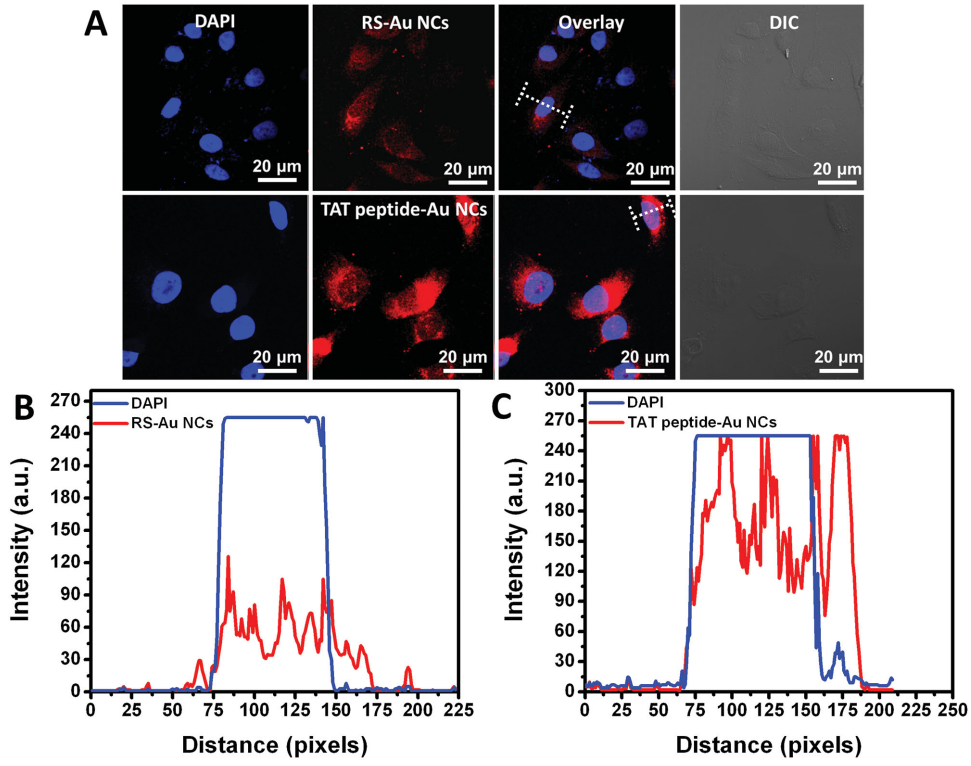


**Figure 3.** A) Confocal fluorescence images for photoexcitation of internalized red emitting RS–Au NCs and TAT peptide–Au NCs in HeLa cells by 533 nm excitation light. The fluorescence emission was monitored from the red channel ($\lambda_{em}$ = 570–630 nm). The nucleus of HeLa cell was stained with blue fluorescent DAPI dye by 404 nm excitation light. B,C) The line profiles for DAPI, RS–Au NCs and TAT peptide–Au NCs were obtained from the dashed white lines represented in (A).

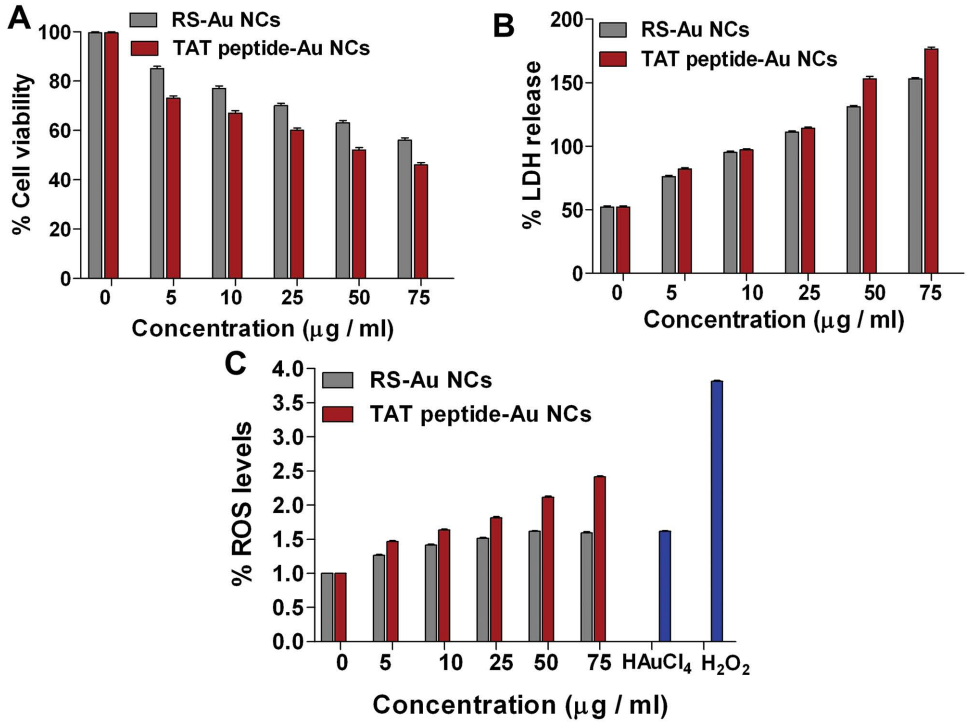


**Figure 4.** In vitro cytotoxicity of RS–Au NCs and TAT peptide–Au NCs A) MTT cell viabilities and B) percentages of LDH levels. C) ROS generation monitored for various concentrations of RS–Au NCs and TAT peptide–Au NCs in HeLa cells for 3 h and the mean fluorescence intensities of DCF were quantified. Pretreatment of cells with 0.01 M $HAuCl_4$ was served as a control and $10 \times 10^{-6}$ M $H_2O_2$ was served as a positive control, respectively.

be oxidized by intracellular ROS to become highly fluorescent 2,7-dichlorofuorescein (DCF). HeLa cells were treated with various concentrations of RS–Au NCs and TAT peptide–Au NCs for 3 h under reduced serum conditions. Figure 4C clearly indicates that the ROS levels induced by TAT peptide–Au NCs in HeLa cells are slightly higher than those of RS–Au NCs as well as $HAuCl_4$. Overall, our in vitro cellular uptake and cytotoxicity results suggest that TAT peptide–Au NCs can be efficiently internalized by HeLa cells with the majority of the fraction being entered into the nucleus without causing any significant cytotoxic effects.

### 2.3. In Vitro Gene Delivery Using Lipid-Coated Au Nanoclusters

Gene delivery is an effective therapeutic treatment modality to cure many incurable diseases. In addition to the virus-based vectors, nonviral vectors, such as liposomes, dendrimers, and cationic polymers, are also widely used to carry genes. However, the abovementioned nonviral vectors suffer from severe cytotoxicity and poor gene delivery efficiencies.[29] Recently, many new nanomaterials, such as gold nanoparticles, graphene, carbon nanotubes, silica nanoparticles, quantum dots, etc., were reported to act as gene delivery vectors to carry DNA/siRNA.[29] Most of the nanomaterial-based nonviral vectors suffer from poor intracellular uptake and inefficient gene release, which results in very poor gene transfection efficiencies. By keeping the above limitations in mind, ideally one has to design nanomaterials with small sizes so that they can possess ultrahigh intracellular uptake, less toxicity, excellent gene loading capacity, and very good delivery efficiency.[29,30] In general, positively charged gene delivery vectors can effectively form complexes with polyanionic DNAs via electrostatic attraction. Hence, the zeta-potentials for RS–Au NCs and TAT peptide–Au NCs were measured in the presence of phosphate buffer solution (PBS) buffer solution (Figure S7, Supporting Information). The as synthesized RS–Au NCs exhibit negative charge and upon conjugation with the TAT peptide, the surface charge turns to positive. After complexation of RS–Au NCs or TAT peptide–Au NCs with pDNA, the surface charge becomes negative, as the pDNA concentration was increased. To fulfill the above needs, the gene transfection efficiencies in HeLa cells pretreated with the current pDNA–RS–Au NCs and pDNA–TAT peptide–Au NCs were evaluated. After 3 h uptake, the free pDNA–RS–Au NCs and pDNA–TAT peptide–Au NCs were washed away and the HeLa cells were allowed to incubate for additional 20 h. The fluorescence property of RS–Au NCs and TAT peptide–Au NCs allows us to track the exact location of the nanoparticles using CLSM. **Figure 5**A shows that the red fluorescence originated from both pDNA–RS–Au NCs and pDNA–TAT peptide–Au NCs. The red fluorescence from the pDNA–RS–Au NCs and pDNA–TAT peptide–Au NCs were clearly overlapped with the green fluorescent protein (GFP) expression. In addition, the cellular uptake and gene transfection efficiencies were also monitored for the HeLa cells fed with pDNA–lipid-coated Au nanoclusters at different DNA-to-nanocarrier charge ratio using flow cytometry (see Figures 5B and S6, Supporting Information). The gene transfection efficiency gradually increases with the increase in the DNA-to-nanocarrier charge ratio. In sharp contrast, ≈64% and ≈81%

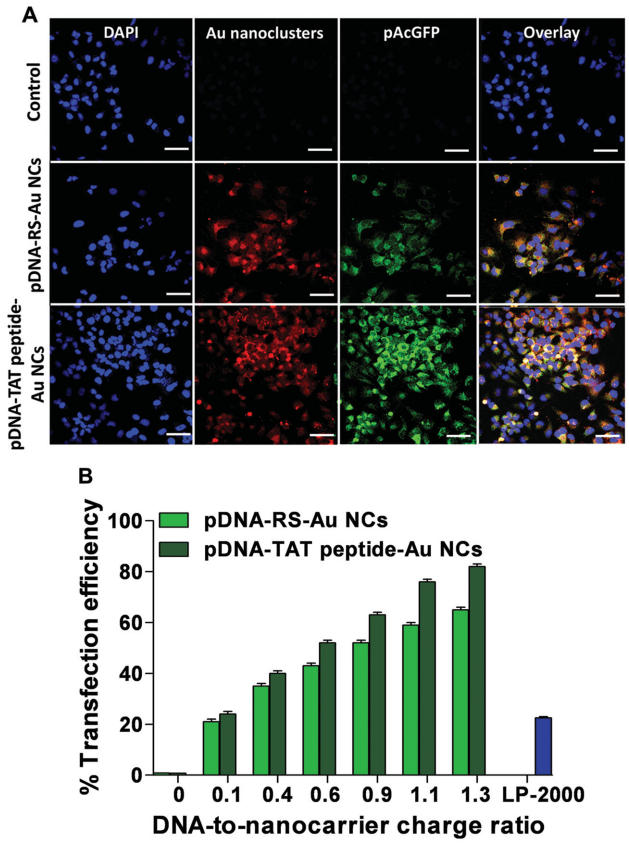


**Figure 5.** A) Confocal laser scanning optical images of HeLa cells at 20 h after internalized with pDNA–RS–Au NCs and pDNA–TAT peptide–Au NCs, respectively. The DNA-to-nanocarrier charge ratio is 1.1. The green fluorescence was from GFP and the red fluorescence from RS–Au NCs and TAT peptide–Au NCs. The HeLa cell nucleus was stained with DAPI dye. B) The percentages of gene transfection efficiency of pDNA–RS–Au NCs and pDNA–TAT peptide–Au NCs complexes monitored using flow cytometry.

gene transfection efficiencies were observed for pDNA–RS–Au NCs and pDNA–TAT peptide–Au NCs at a DNA-to-nanocarrier charge ratio of 1.5. However, only ≈22% gene transfection efficiency was observed using LP-2000, which are ≈3.2 times lower than that obtained RS–Au NCs and TAT peptide–Au NCs as carriers. The gene transfection efficiency results of lipid-coated Au nanoclusters are similar to that for lipid-Fe@CNPs.[31] Overall the results in Figure 5 clearly demonstrate that RS–Au NCs and TAT peptide–Au NCs can facilitate ultrahigh cellular uptake and gene transfection efficiencies, which can pave the way for the development of highly biocompatible and efficient nanocarriers for gene delivery applications.

### 2.4. In Vivo Fluorescence Tracking, Gene Delivery and Cytotoxicity Using RS–Au NCs and TAT peptide–Au NCs in Zebrafish

Zebrafish (*Danio rerio*) is a robust and excellent animal model for in vivo imaging and biocompatibility evaluations of nanomaterials, owing to its high optical transparency, similarity to mammals, such as mouse, rat, and humans as well as its very easy maintenance.[30,31] These intriguing features of zebrafish can offer direct detection of abnormalities or malformations. From **Figure 6**A, the confocal laser scanning optical microscopy images of pDNA–RS–Au NCs microinjected zebrafish reveals that the distribution of GFP gene and the location of RS–Au NCs were totally different. The location of RS–Au NCs (red fluorescence signals) was at the yolk-sac region, whereas the distribution of GFP gene (green fluorescence signals) is throughout the whole body of the zebrafish. This clearly indicates that the plasmid DNA molecules from pDNA–RS–Au NCs complexes were able to detach from the surface of RS–Au NCs very efficiently. However, the confocal images of pDNA–TAT peptide–Au NCs complexes microinjected zebrafish also exhibited a very good detachability of GFP gene from

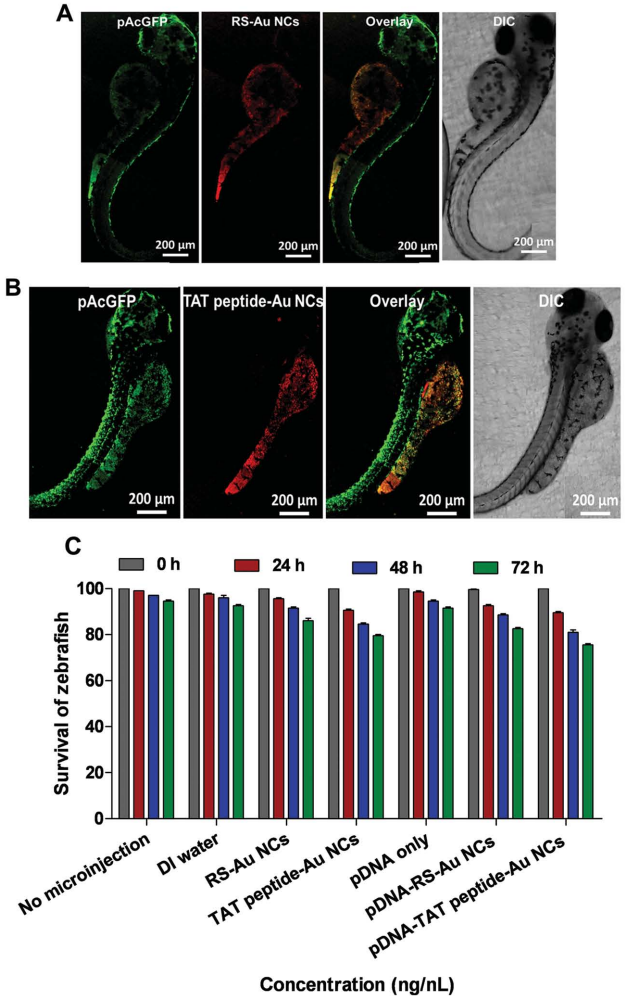


**Figure 6.** A,B) In vivo gene expression in zebrafish using pDNA–RS–Au NCs and pDNA–TAT peptide–Au NCs monitored by confocal laser scanning optical microscopy. The images were recorded at 10× magnification for 72 hpf. The green fluorescence was observed from GFP ($\lambda_{ex}$ = 488 nm, $\lambda_{em}$ = 505–540 nm) and red fluorescence ($\lambda_{ex}$ = 533 nm, $\lambda_{em}$ = 570–630 nm) was derived from RS–Au NCs and TAT peptide–Au NCs, respectively. C) Survival rates of zebrafish after microinjection of RS–Au NCs, TAT peptide–Au NCs, pDNA–RS–Au NCs and pDNA–TAT peptide–Au NCs, respectively, at different hpf.

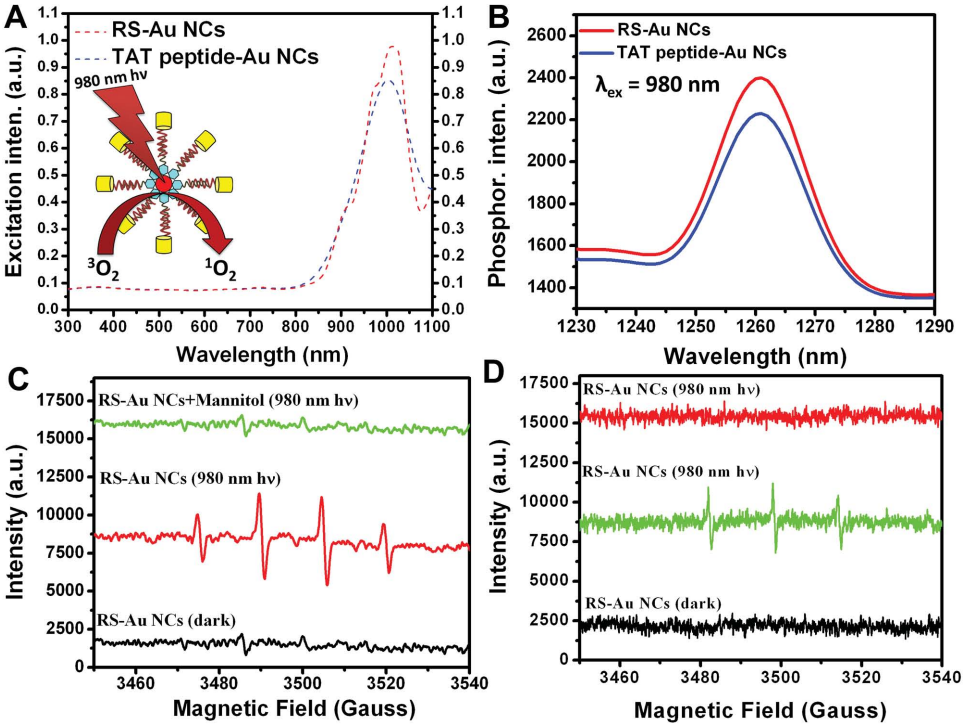


**Figure 7.** A) Excitation spectrum for singlet oxygen phosphorescence of RS–Au NCs and TAT peptide–Au NCs ($\lambda_{em}$ = 1261 nm). B) Singlet oxygen phosphorescence emission spectra of RS–Au NCs and TAT peptide–Au NCs at 980 nm excitation wavelength. EPR spectra of two main ROS spin adducts generated by RS–Au NCs under irradiation by a 980 nm CW laser with a power intensity of 1 W cm$^{-2}$ for 5 min. C) DMPO-OH adducts in aqueous solution containing 0.1 M DMPO; the concentration of ROS scavenger used is $10 \times 10^{-3}$ M Mannitol. D) TEMP-$^1O_2$ adducts in $D_2O$ solution containing 0.3 M TEMP; the concentration of ROS scavenger used is $10 \times 10^{-3}$ M L-histidine. Control experiments were performed for the RS–Au NCs alone without light (black curves).

the surface of pDNA–TAT peptide–Au NCs complexes (see Figure 6B). In addition, the distribution of GFP gene was also seen in the floor plates and blood vessels of the zebrafish microinjected with pDNA–TAT peptide–Au NCs complexes but not with pDNA–RS–Au NCs. The fluorescence microscopy images of zebrafish at different hours postfertilization (hpf) clearly reveals the levels of GFP gene expression of naked DNA, pDNA–RS–Au NCs, and pDNA–TAT peptide–Au NCs, respectively (see Figure S8A, Supporting Information). It was clearly evident that the GFP level for pDNA–TAT peptide–Au NCs is approximately threefold higher than those from the free naked DNA and the pDNA–RS–Au NCs systems (see Figure S8B, Supporting Information). Overall, the in vivo gene expression results clearly suggest that TAT peptide–Au NCs is an excellent nanocarrier demonstrating effective DNA release with high gene transfection efficiencies.

To study the in vivo cytotoxicities of RS–Au NCs, TAT peptide–Au NCs, free naked DNA, pDNA–RS–Au NCs and pDNA–TAT peptide–Au NCs complexes on the embryonic development of zebrafish, different doses of nanocargoes were microinjected into the eight-cell stage of zebrafish embryoes. From Figure 6C, it is very clear that RS–Au NCs, TAT peptide–Au NCs, naked DNA, pDNA–RS–Au NCs and pDNA–TAT peptide–Au NCs exhibit concentration dependent behavior on the survival rates of the zebrafish. Control experiments were also performed by microinjecting double-distillated water, and a set of embryos without microinjection; and the survival rates of zebrafish were compared under identical experimental conditions. The in vivo toxicity effects of RS–Au NCs and TAT peptide–Au NCs are similar to that of the literature reported nanomaterials, such as silver nanoparticles (Ag NPs), iron oxide nanoparticles, iron core–shell carbon nanoparticles (Fe@CNPs) and nanodiamonds (NDs).[32–35] Taken together, these results suggest that RS–Au NCs and TAT peptide–Au NCs as nano-DNA cargoes were considered to be very promising with low cytotoxicity in both in vitro and in vivo systems.

### 2.5. In Vitro Nucleus-Targeting Photodynamic Therapy Using RS–Au NCs and TAT Peptide–Au NCs

The UV–vis–NIR absorption spectra clearly reveals that the RS–Au NCs and TAT peptide–Au NCs show maximum absorption in the UV and visible regions with a tail extending up to NIR region (see Figure 2A). In addition to the appreciable UV–vis–NIR absorption, we also observe that RS–Au NCs and TAT peptide–Au NCs can sensitize the formation of singlet oxygen upon long NIR light (850–1100 nm) photoexcitation. The excitation spectrum for singlet $O_2$ phosphorescence emission clearly reveals a characteristic peak centered at a wavelength of ≈980 nm (see dashed lines in **Figure 7**A). Singlet $O_2$ can only be formed when excited by long NIR light (850–1100 nm). The data in Figure 7B clearly reveal that upon excitation using 980 nm light, a very clear cut singlet

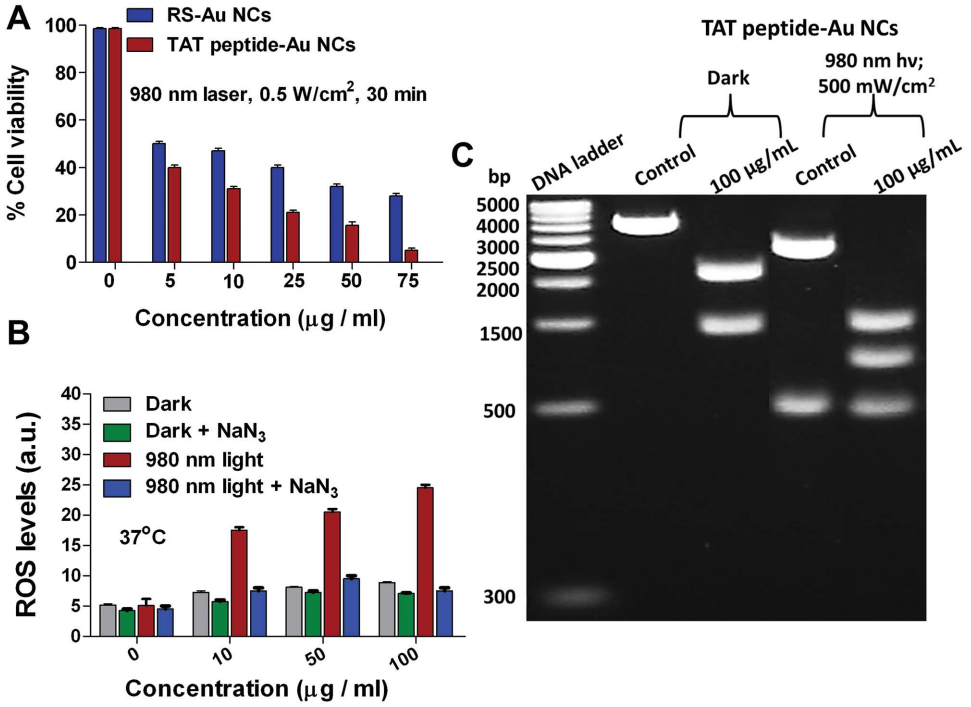


**Figure 8.** A) Cell viabilities of RS–Au NCs and TAT peptide–Au NCs internalized HeLa cells under photoirradiation conditions at 37 °C. B) ROS generation monitored by the mean fluorescence using flow cytometry for TAT peptide–Au NCs internalized HeLa cells followed by photoirradiation with and without $NaN_3$ pretreatment. C) DNA fragmentation assay monitored using gel electrophoresis for TAT peptide–Au NCs internalized HeLa cells under dark and photoirradiation conditions.

$O_2$ phosphorescence emission was detected at ≈1261 nm. The quantum yields for sensitization of singlet oxygen by RS–Au NCs and TAT peptide–Au NCs at 980 nm light excitation are 0.048 and 0.046, respectively (see supplementary information for details and also Table S1 (Supporting Information) for the comparison of the quantum yields for singlet oxygen from various surface modified gold nanoclusters reported in the literature).

In addition to the observation of singlet $O_2$ phosphorescence emission upon 980 nm light excitation of RS–Au NCs, we have also detected the oxygen-centered radicals, such as ·OH and $^1O_2$ using electron paramagnetic resonance (EPR) spectroscopy. As shown in Figure 7C, the 980 nm photoexcitation of RS–Au NCs and 5,5-dimethyl-1-pyrroline *n*-oxide (DMPO) solution leads to the formation of DMPO-OH spin adducts (red curve). The production of ·OH was further suppressed upon addition of $10 \times 10^{-3}$ M mannitol (a known ·OH radical quencher). However, in the dark, no significant ·OH radical signal was detected. To detect $^1O_2$ using EPR, we have used 2,2,6,6-tetramethyl-4-piperidone (TEMP) as a spin-trapping reagent (see Figure 7D). The EPR signal for the photoexcited $O_2$-saturated RS–Au NCs dispersion clearly displayed a characteristic 1:1:1 triplet line to form a TEMPO (TEMP-$^1O_2$) spin adduct.[36] In contrast, no singlet oxygen signal was detected in the dark (black curve). To further look for evidences regarding the involvement of the singlet $O_2$ during the photosensitization process, a specific $^1O_2$ scavenger, histidine was employed. The intensity of the EPR signal was remarkably suppressed in the presence of $10 \times 10^{-3}$ M histidine (red curve).[36] Overall, it is very clear that upon photoexcitation using 980 nm light, RS–Au NCs can effectively sensitize formation of singlet oxygen, as evidenced by both the direct observation of phosphorescence emission and EPR measurements.

To demonstrate that gold nanoclusters can act as NIR light activatable and nucleus targeting PDT reagents in the in vitro cellular level, RS–Au NCs or TAT peptide–Au NCs were fed to the HeLa cells and irradiated with 980 nm CW laser (500 mW $cm^{-2}$; 30 min). The RS–Au NCs and TAT peptide–Au NCs internalized HeLa cells did not induce any significant cytotoxicity in the dark (see Figure 4A). Upon photoirradiation by 980 nm light, a significant drop in the cellular viabilities were observed (for example, at 75 μg $mL^{-1}$ concentration, the cellular viabilities of RS–Au NCs and TAT peptide–Au NCs internalized HeLa cells are 28% and 5%, respectively) (see **Figure 8**A). Precisely, the overall percentage of photoinduced cellular deaths were 28% and 41% at 75 μg $mL^{-1}$ concentration of RS–Au NCs and TAT peptide–Au NCs (% photoinduced cellular death = % cell viability in the dark – % cell viability upon photoirradiation). To look at the deeper insight into the cellular deaths by TAT peptide–Au NCs irradiated with 980 nm light, we have also measured the intracellular levels of ROS. To further confirm the precise role of singlet $O_2$, the amounts of ROS levels were measured with and without pretreatment of a singlet $O_2$ quencher, sodium azide ($NaN_3$).[23–25] From Figure 8B, the amounts of ROS generated from the TAT peptide–Au NCs internalized HeLa cells by 980 nm light are far higher than those generated in the dark. In addition, the pretreatment of HeLa cells with sodium azide significantly suppressed the ROS levels in the case of 980 nm light irradiation. These results clearly support that under 980 nm light photoirradiation, TAT

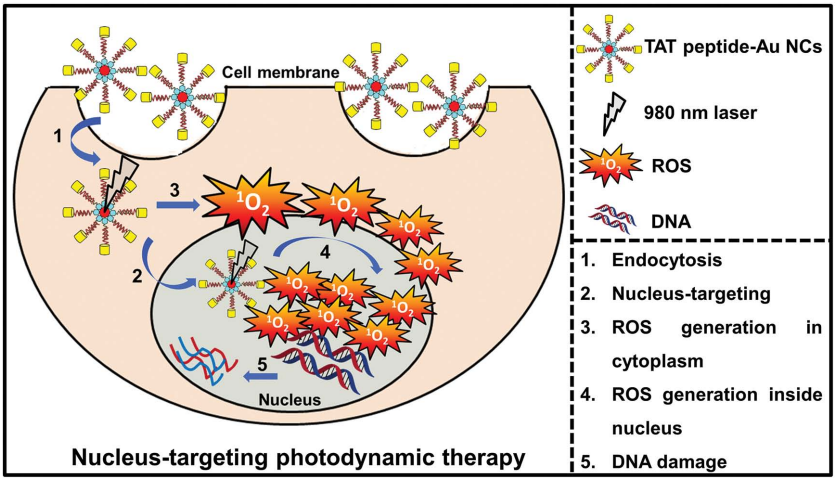


**Scheme 1.** Schematic representation for the nucleus-targeting TAT peptide–Au NCs mediated photodynamic therapy.

peptide–Au NCs induce much higher ROS levels which leads to the significant cellular deaths. In the recent scenario, the currently used photodynamic therapeutic treatments are not considered to be that much effective, since they cannot target and damage the DNA. The unique property of TAT peptide–Au NCs is that they can colocalize inside the nucleus very efficiently. Therefore, upon NIR light exposure, it is expected that the nucleus targeting TAT peptide–Au NCs can induce damage to the DNA. To verify the effectiveness of photoinduced damage of DNA in the present study, the TAT peptide–Au NCs internalized HeLa cells were irradiated with the 980 nm laser and then the DNA inside the HeLa cells were systematically isolated by following a well-established literature protocol.[37] The results from the gel electrophoresis on 1% agarose gel with ethidium bromide staining in Figure 8C showed that the TAT peptide–Au NCs caused effective photoinduced oxidative damage of DNA (with three intense bands). In contrast, the cells without any pretreatment and the TAT peptide–Au NCs internalized HeLa cells in the dark do not exhibit significant DNA cleavage.

Although, the light absorbing capability of TAT peptide–Au NCs is low in the NIR region, nevertheless, their efficiency to target nucleus and damage DNA are highly promising (see **Scheme 1**). Despite of numerous studies being reported on organic photosensitizer-mediated PDT for the destruction of cancer cells or solid tumors, the nucleus targeting photodynamic therapeutic reagents are still very rare. Previously, it was reported that $Au_{25}$ $(SR)_{18}$ can sensitize formation of singlet oxygen upon visible light (532 and 650 nm) and short NIR light (808 nm) excitation via energy transfer from $Au_{25}$ $(SR)_{18}^{-}$ to molecular oxygen.[22] The authors also simply attributed that the observed photoinduced cellular deaths were solely due to singlet $O_2$ without reporting any supporting evidences, such as detection of ROS and subsequent sodium azide quenching inside cells. In this study, we present the generation of singlet $O_2$ from RS–Au NCs and TAT peptide–Au NCs with long NIR light (980 nm) (see the excitation spectrum for singlet $O_2$ phosphorescence in Figure 7B). Longer wavelength excitable nanomaterials are usually attractive as they promise effective therapeutic treatment of deep-tissue buried tumors in the clinics. In addition, we have also detected higher ROS levels inside TAT peptide–Au NCs internalized HeLa cells upon photoexcitation of 980 nm light. The subsequent sodium azide quenching experiments clearly confirmed that the primary source of ROS observed inside HeLa cells is singlet $O_2$. Moreover, the nucleus targeting ability and photoinduced DNA damage of TAT peptide–Au NCs internalized HeLa cells were not yet reported in the literature. The current RS–Au NCs and TAT peptide–Au NCs have several advantages when compared to the literature reported Ce6-conjugated Au NCs as photosensitizers for PDT, such as (a) superior light absorption than organic photosensitizers, (b) excellent photostabilities, (c) resistant to enzymatic degradation, and (d) photoexcitation by longer wavelengths (980 nm), which can promise the treatment of deep tissue buried solid tumors. It is literally impossible using these literature reported organic photosensitizer-conjugated Au NCs system to treat deep tissue-buried solid tumors due to the poor light penetration depths of UV–vis excitation light.[38]

In addition, the nucleus targeting TAT peptide–Au NCs can act as an excellent photoprodrug, in which the cancer cells can be effectively destructed only in the presence of light and molecular oxygen. If the consumption of the molecular oxygen has reached the saturation threshold level, then the photoprodrug action can be completely diminished. In such cases, a time lapse in the photoirradiation can help to regain enough molecular oxygen to further proceed with the killing of cancerous cells. Such kind of photoprodrug mechanism, however, will not work in the conventional chemotherapeutic treatments. Nucleus-targeting nanomaterials is very rare and unique.[39,40] Although, gold nanoparticles, mesoporous silica nanoparticles, and magnetic nanoparticles modified with NLS peptides were known to enter into the cell nucleus, their larger nanoparticle hydrodynamic sizes can severely limit the efficiency of nucleus targeting.[39–42] Therefore, it is highly desired to develop ultrasmall size nanoparticles/nanoclusters system which can target the cell nucleus very efficiently. Overall, the current nucleus-targeting TAT peptide–Au NCs could certainly meet the above-mentioned criterion and served as multifunctional theranostic reagents for simultaneous fluorescence imaging, gene delivery with ultrahigh gene transfection efficiencies and nucleus targeting photodynamic therapy for successful destruction of cancer cells.

## 3. Conclusion

In summary, we have developed a unique design of nucleus-targeting multifunctional gold nanoclusters-based theranostic nanoplatform capable of performing simultaneous fluorescence imaging, gene delivery and long (850–1100 nm) NIR light-activated photodynamic therapy for the destruction of cancer cells. The TAT peptide–Au NCs exhibit excellent photostabilities, and appreciable biocompatibility in HeLa cells as well as in vivo

zebrafish model system. The red fluorescence emitting TAT peptide–Au NCs also showed excellent colocalization and distribution in the cytoplasm with the significant fraction (>50%) entering into the nucleus of HeLa cells. In addition, TAT peptide–Au NCs can also serve as DNA delivery cargoes with ultrahigh cellular uptake (≈90%) and (≈80%) gene transfection efficiencies in HeLa cells. The percentage of gene transfection using TAT peptide–Au NCs is nearly 3.2-fold higher than that obtained using the most commonly adopted LP2000 liposome gene carrier. The TAT peptide–Au NCs can also sensitize formation of singlet oxygen upon long NIR light (850–1100 nm) excitation without the use of organic photosensitizers. Upon photoexcitation of 980 nm NIR light, the TAT peptide–Au NCs internalized HeLa cells exert effective nucleus-targeting photodynamic therapeutic effects on destruction of cancer cells via photoinduced DNA damages, which is evidenced by the photoinduced DNA cleavage experiments. To the best of our knowledge, the current TAT peptide–Au NCs is the first literature example of multifunctional theranostic reagent that is able to perform simultaneously imaging-guided gene therapy and nucleus targeting NmPDT for the efficient destruction of cancer cells.

## 4. Experimental Section

*Synthesis of Au Nanoclusters (RS–Au NCs)*: A 4 mL of 0.025 M cetyltrimethyl ammonium chloride in toluene and 4 mL of 0.025 M tetraethyl ammonium bromide in butanol were initially premixed and then vigorously stirred for 10 min. A 1 mL of 0.01 M $HAuCl_4$ aqueous solution, in which the pH was adjusted to ≈3.5, was injected into the mixture and within a few seconds solution color turned to orange and then further stirred for another 10 min. 4 mL of 0.28 M of 11-mercaptoundecanoic acid in butanol was then added into the above solution and the color of the solution changed from orange to slight opaque white. Finally, the reaction contents were stirred for another 60 min. The as obtained solution exhibited red fluorescence under UV light (365 nm) excitation.

*Synthesis of TAT Peptide–Au Nanoclusters*: In a typical experiment, 8 mg of EDC, 4 mg of Sulfo-*N*-hydroxy succinimide and 5 mg of TAT peptide (peptide sequence: N-GRKKRRQRRR-C, MB proteomics, Taiwan) were mixed in 500 µL of 0.1 M 4-2-hydroxyethyl)-1-piperazineethane sulfonic acid (HEPES) buffer solution (pH ≈7.2) for 30 min. Now, 10 mg of RS–Au NCs dispersed in 1.5 mL of 0.1 M HEPES buffer solution was further added and constantly stirred for another 24 h. After 24 h, the contents were centrifuged at 12 000 rpm for 5 min and then the residue was redispersed in 5 mL of deionized water to form TAT peptide–Au NCs.

*Singlet Oxygen Phosphorescence Measurements*: For singlet $O_2$ sensitization experiments, aliquots of RS–Au NCs and TAT peptide–Au NCs (1 mg/3 mL) were dispersed in $D_2O$. Phosphorescence emission of singlet $O_2$ was recorded using luminescence spectrometer (FLS920, Edinburgh, equipped with a 450 W broadband Xe lamp) with a 1000 nm longpass filter (Iszu Optics, LP1000) located inbetween the sample and the detector to cut off both the scattering light and stray light having wavelengths shorter than 1000 nm.

*EPR Measurements*: For the detection of $^1O_2$ using EPR, 500 µL of 1 mg $mL^{-1}$ RS–Au NCs in $D_2O$ suspension was added to the 40 µL of 1.0 M TEMP in $D_2O$ solution, and the resulting solution was mixed well. The mixture was then bubbled with $O_2$ for 5 min and then irradiated with 980 nm laser with the power intensity of 1 W $cm^{-2}$ right in front of the EPR spectrometer during the measurements. $10 \times 10^{-3}$ M histidine was used as a scavenger for $^1O_2$ in these experiments. Parameter settings: microwave power, 10.12 mW; frequency, 9.8 GHz; time constant, 40.96 ms; scan width, 100 G.

For the detection of ·OH using EPR, 500 µL of 1 mg $mL^{-1}$ RS–Au NCs aqueous suspension was added to the 40 µL of 1.0 M DMPO in $H_2O$ solution and the resulting solution was mixed well. The mixture was then irradiated with 980 nm laser with the power intensity of 1 W $cm^{-2}$ right in front of the EPR spectrometer during the measurements. $10 \times 10^{-3}$ M Mannitol was used as a scavenger for ·OH in these experiments.

*Cell Cultures*: HeLa (human cervical cancer cells) were grown in Dulbecco's modified Eagle medium (DMEM, Gibco, USA) supplemented with 10% fetal bovine serum (FBS) (Invitrogen, Carlsbad, CA, USA), $2 \times 10^{-3}$ M L-glutamine, 100 µg $mL^{-1}$ penicillin and 100 U $mL^{-1}$ streptomycin, placed and grown in a humidified incubator at 37 °C (95% humidity, 5% $CO_2$).

*Cytotoxicity Assay (MTT)*: In a 24-well plate, 1 mL of HeLa cell-containing solution with the cell density of $\approx 2 \times 10^4$ cells $mL^{-1}$ was added to each well and incubated for 1 d to allow cells to stick on the surface of the plate. Different aliquots of RS–Au NCs and TAT peptide–Au NCs were added to the 24-well plate, and the cell solutions were incubated for another 2 d. A 50 µL amount of a MTT aqueous solution (0.5 mg $mL^{-1}$) was added to each well of the 24-well plate 4 h before termination of the 3 d incubation, and the cells were allowed to incubate for another 4 h. Then, the upper layer of the solutions in the 24-well plate was discarded, and 1 mL of dimethyl sulphoxide (DMSO) was added to each well to lyse cell membrane followed by pipette stirring. The final solution in each well was centrifuged at 13 000 rpm to remove any solid residues before measurements of the optical absorbance at 570 nm. The optical absorbances were converted to cell viabilities based on a standard curve (absorbance vs. cell numbers) obtained from controlled experiments carried out under the same condition except that no nanoparticles were added during cell culture processes.

*LDH Release Assay*: $2 \times 10^4$ cells $mL^{-1}$ were loaded in a 24-well plate and incubated for 24 h. Different aliquots of RS–Au NCs and TAT peptide–Au NCs were added and further allowed it to interact for another 24 h. The cells were washed with PBS, trypsinized and centrifuged at 13 000 rpm. 100 µL of the supernatant was transferred into another 96-well plate. To this, 100 µL of LDH reaction solution (Clontech Cytotoxicity Detection Kit, USA) was added and incubated for 30 min in the dark at room temperature. Before colorimetric detection at 490 nm, 1 N HCl was added to stop the enzymatic reaction.

*Cellular Uptake Experiments*: For confocal experiments, HeLa cells ($2.0 \times 10^5$ cells per well in six-well plate) cultured in DMEM and treated with different aliquots of RS–Au NCs and TAT peptide–Au NCs for 3 h. The cells were washed with a PBS (pH 7.4), further fixed onto a glass slide using paraformaldehyde solution (4%) in PBS for 5 min, and washed with PBST (5% Tween-20 in phosphate buffer solution) solution for three times. The cells were stained with DAPI (4′,6-diamidino-2-phenylindole, 1 ng $mL^{-1}$ PBS, 30 min) and examined under a CLSM (Leica, TCS SP5X) equipped with an InGaN semiconductor laser (405 nm), an Ar laser (488 nm), and a He–Ne laser (533 nm). During measurements, a 63 X objective lens was used with a spatial resolution of ≈200 nm in *x*–*y* direction and ≈100 nm in *z*-direction. For flow cytometry experiments, the cells feeded with clusters were trypsinized and resuspended in 1 mL PBS buffer and further the fluorescence was quantified for 10 000 cells from propidium iodide (PI) channels.

*ROS Assay*: HeLa cells were seeded into six-well plate with the cell number of $2 \times 10^5$ cells per well. After 24 h, different concentrations of RS–Au NCs and TAT peptide–Au NCs were added into the cells and incubated for additional 3 h under serum-free conditions. For control experiments, the gold precursor, 0.01 M $HAuCl_4$ was also added to the cells under identical conditions as that of lipid-coated Au nanoclusters. The cells were washed with PBS and replaced with serum containing medium along with DCFH-DA solution ($5 \times 10^{-6}$ M in cell culture medium) were added and incubated for 30 min at 37 °C. As a positive control, $5 \times 10^{-6}$ M $H_2O_2$ was also added to the cells and incubated for 30 min. Cells were then trypsinized and aspirated, followed by flow cytometry analysis (BD FACS Canto) equipped with 488 nm laser. Green fluorescence was monitored using FITC channel.

*Microinjection of RS–Au NCs and TAT Peptide–Au NCs into Zebrafish Embryos*: *Danio rerio* (zebrafish) embryos obtained from zebrafish

core facility center, National Tsing Hua University, were used in all the experiments. Fresh embryos were collected onto the microinjection embryo tray just before the experiment. The RS–Au NCs and TAT peptide–Au NCs stock solutions were diluted to appropriate concentrations in double distilled water and sonicated until microinjection. Approximately 10 nL volume was microinjected into the zebrafish pole region of embryos between stages 1 (one cell embryo) and 3 (four cell embryo) using Drummond microinjector. Each experiment was performed on 50 embryos per condition. Following microinjection, embryos were transferred onto the petri dish filled with the system water and incubated at 28 °C in dark. For the in vivo cytotoxicity measurements, the live embryos were counted each day until 72 hpf (hours postfertilization). After 72 hpf, all the developed embryos were hatched manually and examined the types of abnormalities undergone through fluorescence microscope (Nikon, E600). For in vivo imaging experiments, the zebrafish embryos (72 hpf) were hatched and fixed on the cover slips (15 mm × 16 mm, GeneFrame) with 1% agarose gel (Sigma, USA) to monitor the fluorescence of gold nanoclusters using CLSM (10×, LSM-700, Zeiss).

*Preparation of pDNA–RS–Au NCs and pDNA-TAT Peptide–Au NCs Complexes*: Different concentrations of DNA plasmids were diluted with PBS buffer and 10 μg $mL^{-1}$ of RS–Au NCs or TAT peptide–Au NCs were added and vortexed for 10 s and then incubated at 37 °C for 30 min to get stabilized. Then these complexes were further subjected to the cells for the transfection assay experiments.

*Transfection and Cellular Uptake Assay*: Transfection and cellular uptake experiments were carried out procedures using as described elsewhere. HeLa cells were cultured in six-well plates at an initial density of $2 \times 10^5$ cells per well. It was 60% confluent on the day of transfection. After 24 h seeding, the cells were washed with PBS, and then 2 mL of the serum-free DMEM was added to each well. Finally, the cells were transfected with the pDNA–RS–Au NCs or pDNA–TAT peptide–Au NCs complexes for 3 h. After 3 h incubation (duration of transfection) at 37 °C (under 5% $CO_2$), the medium was changed to DMEM supplemented with 10% FBS and further incubated for 24 h. After 24 h incubation the cells were washed with PBS buffer and trypsinized with 1 mL trypsin and centrifuged at 1000 rpm for 5 min. Finally the cells were resuspended in 1 mL fresh PBS solution and then subjected to flow cytometry analysis to examine the fluorescence in the green and red channels, respectively.

*In Vitro NmPDT Experiments*: HeLa cells ($2.0 \times 10^4$ cells $mL^{-1}$) were cultured in a 24-well plate and incubated for 1 d to allow cells to stick onto the surface of the plate. Different concentrations of RS–Au NCs and TAT peptide–Au NCs were added to the 24-well plate and the cell solutions were incubated in dark at 37 °C for 3 h. To determine the phototoxicities of RS–Au NCs and TAT peptide–Au NCs, HeLa cells were irradiated with 980 nm laser (500 mW $cm^{-2}$; 30 min). After irradiation, the cells were further incubated at 37 °C for another 12 h. A 50 μL amount of a MTT aqueous solution (0.5 mg $mL^{-1}$) was added to each well of the 24-well plate at 4 h before termination of the incubation, and the cells were allowed to incubate for another 4 h. Then, the upper layer of the solutions in the 24-well plate was discarded, and 1 mL of DMSO was added to each well to lyse cell membrane followed by pipette stirring. The final solution in each well was centrifuged at 13 000 rpm to remove any solid residues before measurements of the optical absorbance at 570 nm. The optical absorbances were converted to cell viabilities based on a standard curve (absorbance vs cell numbers) obtained from controlled experiments carried out under the same condition except that no nanoparticles were added during cell culture processes. For ROS experiments, the cells were cultured under similar conditions as described for MTT experiments, except that after photoirradiation, the cells were trypsinized and aspirated, followed by flow cytometry analysis by monitoring the green fluorescence using the FITC channel. For $NaN_3$ quenching experiments, HeLa cells were pretreated with $50 \times 10^{-3}$ M $NaN_3$ solution mixed in PBS and incubated for 1 h, followed by photoirradiation and subjected to ROS analysis.

*Isolation of DNA from HeLa Cells*: 2 mL of HeLa cells-containing solution ($2.0 \times 10^6$ cells $mL^{-1}$) was added to each well of a six-well plate and incubated for 1 d to allow cells to stick onto the surface of the plate. Different amounts of TAT peptide–Au NCs were added to the 24-well plate, and the cell solutions were incubated in dark at 37 °C for another 4 h. The cells were then irradiated with 980 nm laser (500 mW $cm^{-2}$; 30 min). After photoirradiation, the cells were washed for three times with PBS and trypsinized and then suspended in ice cold PBS for one time. Then 300 μL cell lysis buffer ($10 \times 10^{-3}$ M Tris HCl + $10 \times 10^{-3}$ M ethylene diamine tetracetic acid (EDTA) + 0.5% Triton) was added to the pellet followed by the addition of 100 μg $mL^{-1}$ proteinase K (Sigma-Aldrich) to remove the proteins. Then the solution was incubated for overnight at 37 °C followed by the addition of 50 μg $mL^{-1}$ RNase A (Invitrogen, USA) and incubated for 4 h at 37 °C. Then 100% absolute ethanol was added so that the total concentration was adjusted to 70%. Invert the tube gently and kept at room temperature for 10 min. The contents were then centrifuged at 12 000 rpm for 5 min. The supernatant was then removed and the white pellet was settled at the bottom of the tube. The residual ethanol was aspirated and 20 μL of doubly distillated water was added and then the DNA concentration and the quality of the isolation were estimated by using Nanodrop.

*DNA Fragmentation Assay*: In a typical experiment, isolated DNA (2 μg) was first mixed with the loading dye along with the DNA marker. Then the mixtures were loaded into a 1.0% agarose gel in tris–acetate–EDTA buffer. The gel was allowed to run for 30 min at 150 V (7.5 V $cm^{-1}$) and then it was photographed under UV light to visualize the DNA fragmentation.

All the animal experiments were carried out in accordance with local regulations and with approval from the Committee of Animal Use Protocol, National Tsing Hua University, Taiwan.

## Supporting Information

Supporting Information is available from the Wiley Online Library or from the author.

## Acknowledgements

The authors are grateful to the financial support from the Ministry of Science and Technology, Taiwan.

Received: June 29, 2015
Revised: July 11, 2015
Published online: August 28, 2015

[1] R. David, M. R. Zimmerman, *Nat. Rev. Cancer* **2010**, *10*, 728.
[2] C.-K. Chan, D. A. Jans, *Immunol. Cell Biol.* **2002**, *80*, 119.
[3] O. Cohen, R. Granek, *Nano Lett.* **2014**, *14*, 2515.
[4] S. Dixit, T. Novak, K. Miller, Y. Zhu, M. E. Kenney, A.-M. Broome, *Nanoscale* **2015**, *7*, 1782.
[5] N.-T. Chen, S.-H. Cheng, J. S. Souris, C.-T. Chen, C.-Y. Mou, L.-W. Lo, *J. Mater. Chem. B* **2013**, *1*, 3128.
[6] Y. Liu, L. Feng, T. Liu, L. Zhang, Y. Yao, D. Yu, L. Wang, N. Zhang, *Nanoscale* **2014**, *6*, 3231.
[7] Y.-P. Ho, K. W. Leong, *Nanoscale* **2010**, *2*, 60.
[8] P. Huang, J. Lin, X. Wang, Z. Wang, C. Zhang, M. He, K. Wang, F. Chen, Z. Li, G. Shen, D. Cui, X. Chen, *Adv. Mater.* **2012**, *24*, 5104.
[9] G. Chen, H. Qiu, P. N. Prasad, X. Chen, *Chem. Rev.* **2014**, *114*, 5161.
[10] M. Montalti, L. Prodi, E. Rampazzo, N. Zaccheroni, *Chem. Soc. Rev.* **2014**, *43*, 4243.
[11] E. Oh, F. K. Fatemi, M. Currie, J. B. Delehanty, T. Pons, A. Fragola, S. Lévêque-Fort, R. Goswami, K. Susumu, A. L. Huston, I. L. Medintz, *Part. Part. Syst. Charact.* **2013**, *30*, 453.
[12] J.-Y. Zhao, R. Cui, Z.-L. Zhang, M. Zhang, Z.-X. Xie, D.-W. Pang, *Nanoscale* **2014**, *6*, 13126.

[13] J. M. Kim, S. H. Sohn, N. S. Han, S. M. Park, J. Kim, J. K. Song, *ChemPhysChem* **2014**, *15*, 2917.
[14] C. Zhang, Z. Zhou, X. Zhi, Y. Ma, K. Wang, Y. Wang, Y. Zhang, H. Fu, W. Jin, F. Pan, D. Cui, *Theranostics* **2015**, *25*, 1314.
[15] D. E. J. G. J. Dolmans, D. Fukumura, R. K. Jain, *Nat. Rev. Cancer* **2003**, *3*, 380.
[16] Z. Huang, *Technol. Cancer Res. Treat.* **2005**, *4*, 283.
[17] A. P. Castano, P. Mroz, M. R. Hamblin, *Nat. Rev. Cancer* **2006**, *6*, 535.
[18] A. A. Rosenkranz, D. A. Jans, A. S. Sobolev, *Immunol. Cell Biol.* **2000**, *78*, 452.
[19] L. Pan, J. Liu, J. Shi, *Adv. Funct. Mater.* **2014**, *24*, 7318.
[20] T. Das, P. Ghosh, M. S. Shanavas, A. Maity, S. Mondal, P. Purkayastha, *Nanoscale* **2012**, *4*, 6018.
[21] M. Sakamoto, T. Tachikawa, M. Fujitsuka, T. Majima, *Langmuir* **2009**, *25*, 13888.
[22] H. Kawasaki, S. Kumar, G. Li, C. Zeng, D. R. Kauffman, J. Yoshimoto, Y. Iwasaki, R. Jin, *Chem. Mater.* **2014**, *26*, 2777.
[23] R. Vankayala, Y.-K. Huang, P. Kalluru, C.-S. Chiang, K. C. Hwang, *Small* **2014**, *10*, 1612.
[24] R. Vankayala, C.-C. Lin, P. Kalluru, C.-S. Chiang, K. C. Hwang, *Biomaterials* **2014**, *35*, 5527.
[25] P. Vijayaraghavan, C.-H. Liu, R. Vankayala, C.-S. Chiang, K. C. Hwang, *Adv. Mater.* **2014**, *26*, 6689.
[26] A. K. Murthy, R. J. Stover, W. G. Hardin, R. Schramm, G. D. Nie, S. Gourisankar, T. M. Truskett, K. V. Sokolov, K. P. Johnston, *J. Am. Chem. Soc.* **2013**, *135*, 7799.
[27] R. Waehler, S. J. Russell, D. T. Curiel, *Nat. Rev. Genet.* **2007**, *8*, 573.
[28] S. L. Ginn, I. E. Alexander, M. L. Edelstein, M. R. Abedi, J. Wixon, *J. Gene Med.* **2013**, *15*, 65.
[29] H.-L. Pu, W.-L. Chiang, B. Maiti, Z.-X. Liao, Y.-C. Ho, M. S. Shim, E.-Y. Chuang, Y. Xia, H.-W. Sung, *ACS Nano* **2014**, *8*, 1213.
[30] R. Vankayala, P. Kalluru, H.-H. Tsai, C.-S. Chiang, K. C. Hwang, *J. Mater. Chem. B* **2014**, *2*, 1038.
[31] R. Vankayala, C.-S. Chiang, J.-I. Chao, C.-J. Yuan, S.-Y. Lin, K. C. Hwang, *Biomaterials* **2014**, *35*, 8261.
[32] K. J. Lee, P. D. Nallathamby, L. M. Browning, C. J. Osgood, X.-H. N. Xu, *ACS Nano* **2007**, *1*, 133.
[33] K. J. Lee, L. M. Browning, P. D. Nallathamby, C. J. Osgood, X.-H. N. Xu, *Nanoscale* **2013**, *5*, 11625.
[34] H. Yin, R. L. Kanasty, A. A. Eltoukhy, A. J. Vegas, J. R. Dorkin, D. G. Anderson, *Nat. Rev. Genet.* **2014**, *15*, 541.
[35] Y. Tao, Z. Li, E. Ju, J. Ren, X. Qu, *Nanoscale* **2013**, *5*, 6154.
[36] L. Gao, R. Liu, F. Gao, Y. Wang, X. Jiang, X. Gao, *ACS Nano* **2014**, *8*, 7260.
[37] S. Peña-Llopis, J. Brugarolas, *Nat. Protoc.* **2013**, *8*, 2240.
[38] C. Zhang, C. Li, Y. Liu, J. Zhang, C. Bao, S. Liang, Q. Wang, Y. Yang, H. Fu, K. Wang, D. Cui, *Adv. Funct. Mater.* **2015**, *25*, 1314.
[39] J.-Y. Zhao, R. Cui, Z.-L. Zhang, M. Zhang, Z.-X. Xie, D.-W. Pang, *Nanoscale* **2014**, *6*, 13126.
[40] Y. Wang, J. Chen, J. Irudayaraj, *ACS Nano* **2011**, *5*, 9718.
[41] L. Pan, Q. He, J. Liu, Y. Chen, M. Ma, L. Zhang, J. Shi, *J. Am. Chem. Soc.* **2012**, *134*, 5722.
[42] C. Xu, J. Xie, N. Kohler, E. G. Walsh, Y. E. Chin, S. Sun, *Chem. Asian J.* **2008**, *3*, 548.